scientific reports

Check for updates

OPEN

Efficient detection of gastric cancer biomarkers on functionalized carbon nanoribbons using DFT analysis

Ibrahim Alghoul[1,2], Tanveer Hussain[3], Shahid Nazir[3] & Nacir Tit[1,2]✉

Early diagnosis of gastric cancer (GC) is crucially important to initiate a therapy plan aiming at rescue and cure. In this regard, the detection of volatile organic compounds (VOCs), related to GC in the patient's exhaled breath, is known to be an efficient and cost-effective technique for early diagnosis. The scope of the present study is to develop a nano-biosensor with great sensitivity and suitable selectivity towards specific VOCs related to GC, such as 2-pentanone, butanone, isoprene, methylglyoxal, N-decanal, N-pentanal, and pyridine. We employed van der Waals corrected density functional theory (DFT) to study the adsorption properties of the mentioned VOCs along with interfering air molecules (N_2, O_2, H_2O, CO_2) using recently synthesized carbon nanoribbons (CNRs). We found that pristine CNRs weakly adsorbed the VOCs with adsorption energies (E_{ads}), which is not suitable for practical sensing applications. However, the incorporation of selected transition metals (Co, Fe, Mn, Ni) in nitrogen-functionalized CNRs (N-CNRs) enhanced the E_{ads} values to -0.802, -0.899, -1.566, -1.260, -1.482, -1.057, and – 0.674 eV for 2-pentanone, butanone, isoprene, methylglyoxal, N-decanal, N-pentanal, and pyridine, respectively. Appropriate E_{ads} values along with distinct variations in the electronic and magnetic properties, measured through band structures, density of states, work function and charge transfer analysis, validated the potential of TM-doped N-CNRs as efficient biosensors towards GC-related VOCs. Consequently, the TM-doped N-CNRs are proposed as candidates for platforms of nano biosensors to detect GC biomarkers with high selectivity.

Gastric cancer (GC) is one of the most common cancers worldwide, ranking fourth in incidence and second as the leading cause of cancer-related deaths worldwide[1]. Over the past several decades many improvements have been made towards timely diagnosis however, GC is often diagnosed at an advanced stage when the prognosis becomes challenging[1]. Annually, GC results in 1.1 million new cases and 770,000 deaths, with projections indicating a rise to approximately 1.8 million new cases and 1.3 million deaths by 2040[2].

The routine diagnostic methods for GC, including gastroscopy and tissue biopsy, are highly invasive and inconvenient for patients[1]. Breathomics (breath analysis/diagnosis) is a rapidly emerging area in diagnosis science and is greatly used to diagnose patients suffering from a variety of diseases including cancer. It is well known that explicit volatile organic compounds (VOCs) are produced in each type of cancer because of certain metabolic and biochemical progressions[2]. Novel pathology indicates that the detection of VOCs should be on the list of early diagnosis of several diseases. Besides, efficient detection of VOCs related to GC is not only a non-invasive method but also a cost-effective and proficient way for the timely diagnosis[2–6].

Considerable research efforts have been focused on both identifying the fingerprints VOCs and developing biosensors with high sensitivity at the order of part per billion (ppb), and operation under ambient conditions. On the experimental side, Mochalski et al. used gas chromatography with mass spectrometric detection to identify VOCs associated with GC, such as carbon disulfide, pyridine, 3-methy-2-butanone and 2-pentanone[7]. Huang et al. used gas chromatography-mass spectrometry with tabular SERS sensor for the detection of eight VOCs, including butanone, methylglyoxal, n-hexanal, n-decanal, cyclohexanone, n-pentanal, n-octanal, and benzaldehyde, with descending order of relevance to GC[8]. Perfecto et al. reported a nanocomposite of ZnO hollow spheres with NiS nanosheets to detect the butanone with high selectivity in a humid environment[9]. Another study by Hong et al. used mass spectrometry to identify seven GC-related VOCs, such as acetone, isoprene, 1,3-dioxolan-2-one, phenol, meta-xylene, 1,2,3-trimethylbenzene, and Phenyl acetate[10]. Very recently,

[1]Department of Physics, College of Science, UAE University, P.O. Box 15551, Al-Ain, United Arab Emirates. [2]National Water and Energy Center, UAE University, P.O. Box 15551, Al-Ain, United Arab Emirates. [3]School of Science and Technology, University of New England, Armidale, NSW 2351, Australia. ✉email: ntit@uaeu.ac.ae

Mochalski et al. presented a more rigorous experimental study on the detection of five VOCs, namely pyridine, ethyl acetate, acetoin, 2,3-butanedione, and 3-methyl-1-butanol, associated with GC[11]. On the computational side, Bac et al. performed ab -initio calculations for the detection of butanone using graphene monolayer[12]. Furthermore, Bhuvaneswari et al. used first-principles calculations for the selective detection of butanone and 2-pentanone on β-Tellurene monolayer[13].

A revolutionary change in materials science occurred in 2004 by Novoselov and Geim[14] in their successful synthesis of a 2D monolayer of graphene using the exfoliation of graphite. The invention not only granted them the Nobel Prize in physics in the year 2010 but also paved the way for the birth of a new world of 2D materials enriched with exciting inventions and discoveries[15]. Many novel fascinating 2D materials (e.g., transition metal dichalcogenides "TMD"[16,17], MXenes[18,19], and porous carbon nitrides[20–22]) have been successfully synthesized. Single atom catalysis (SAC) has proven as a powerful method in tuning the properties of 2D materials towards specific applications, such as electro-catalysis in energy conversion[23–29], gas sensing[30–32], energy storage[33–36], and biosensor applications[37–40].

The idea of exploring selective detection of VOCs was explored in many recent investigations. For instance, recently, the detection of VOCs related to lung cancer was explored using functionalized Ti_3C_2Tx MXenes (T_x = O, F, S, and OH)[41]. The adsorption properties of six VOCs were studied versus those of the interfering air molecules (N_2, O_2, CO_2 and H_2O). The $Ti_3C_2O_2$ MXenes yielded the optimal adsorption selectivity toward the VOCs. Although all the molecules exhibited physisorption-type interactions with the MXenes, the VOCs' adsorption energies were much stronger than those of the interfering air molecules. The strong physisorption coupling was attributed to the enhanced van der Waals (vdW) interactions between the VOCs and the polar surface of $Ti_3C_2O_2$ MXene[41]. The contrast between the VOCs and air molecules is that the polar surface of MXene can induce many electric dipole moments in many localities in the VOCs and, consequently, stronger vdW interactions get triggered. When the vdW interactions become strong enough, they can affect the states at the Fermi level of the substrate to the extent of affecting the transport properties and enhancing the sensor response[41,42].

Recently synthesized, porous carbon nitrides[22] emerged as novel 2D materials with great potential to stably embed transition/light metal atoms in relatively big pores to pave the way for promising hydrogen storage, VOCs' detection, and battery applications. Calculating the cohesive energy, Cai et al.[22] corroborated the experimental stability of many synthesized structures as well as predicted many others to be possible for future synthesis. The authors also demonstrated the relevance of C_3N_2 as a suitable anode material for lithium-ion battery application[22]. Another study led by Kang[43] reported a successful fabrication of carbon-nitride nanoribbon (CNR) composed of 4-5-6-8 membered rings. Subsequently, Mortazavi et al.[44] performed DFT simulations on the same CNR structure in pristine and N-doped forms using HSE06 hybrid functional and reported a direct bandgap energy of 1.25 eV. Of course, the embedment of TM atoms in the pores should metallize the structure as it will be presented in this investigation and that would suit the biosensing applications.

Motivated by the above-mentioned features, we propose exploring TM-SAC embedment in pores of novel N-CNRs to assess the sensing properties of seven VOCs related to GC biomarkers, namely: (i) 2-pentanone "$C_5H_{10}O$", (ii) butanone "C_4H_8O", (iii) isoprene "C_5H_8", (iv) methylglyoxal "$C_3H_4O_2$", (v) n-decanal "$C_{10}H_{20}O$", (vi) n-pentanal "$C_5H_{10}O$", and (vii) pyridine "C_5H_5N". We assess the catalytic responses of embedding four TM-SAC atoms (Mn, Fe, Co, Ni) in N-CNRs for the selective detection of mentioned VOCs as compared to the interfering air molecules (N_2, O_2, H_2O, CO_2) to study the main factors controlling the sensor responses and consequently the selectivity. To the best of our knowledge, this is a pioneer computational work to explore the TM-SAC functionalization of the newly synthesized N-CNRs aiming at the selective detections of VOCs related to GC biomarkers. Toward this aim, we employ the state-of-the-art method, based upon the vdW-corrected spin-polarized DFT, as incorporated in the "Vienna Ab-initio Simulation Package" (VASP). We first demonstrate the stability of TM-SAC embedment in the pores of N-CNRs, then we calculate the spin-polarized bands, partial and total density of states (PDOS & TDOS), charge transfer using Bader charge analysis, and the work function. We will show that the metal doping of N-CNRs would lead to the metallization of N-CNRs and this should suit the biosensing applications. The selective adsorptions of VOCs are corroborated by the adsorption energy and change in electronic and magnetic properties as well as change in work function approaches. The TM-doped N-CNRs will be proven suitable for the detection of GC biomarkers.

Results and discussion

VOCs adsorption on pristine CNRs

The relaxed structure of N-CNRs, spin-polarized band structure and projected density of states are given in Fig. 1a–c, which clearly shows a paramagnetic semiconductor character with a bandgap energy E_g = 0.59 eV, which is consistent with the theoretical value of 0.59 eV reported by Mortazavi[44] using the same GGA-PBE method. It is well known that GGA underestimates E_g and the inclusion of hybrid functional, such as HSE06, can yield the experimental value of 1.40 eV[43]. However, hybrid functional calculations are computationally expensive. The primitive cell has a lattice constant a = 16.190 Å, and a C-C-bond-length of 1.494 Å which are in good agreement with literature[44].

For assessing the active site for the VOCs adsorption on N-CNRs, many positions were considered, as shown in Fig. 2, and the adsorption of nitrogen (N_2) molecule was used for locating the suitable positions. The E_{ads} values on the considered sites are shown in Fig. 2; Table 1. Among all, a large pore (labelled "a" in Fig. 2) with N-CNRs yields the strongest E_{ads} value of -0.547 eV. Therefore, this site is considered for the adsorption of the VOCs and the interfering air molecules. Before adsorption, all the VOCs are relaxed and optimized structures are shown in Fig. S1 (supplementary information), which are consistent with literature[7–13]. Afterwards, atomic relaxations of the VOCs on the N-CNRs are performed by introducing each of the former on site "a" on the latter as shown in Fig. 3. Several possible interactions on N-CNRs with E_{ads} values are shown in Table 1 and

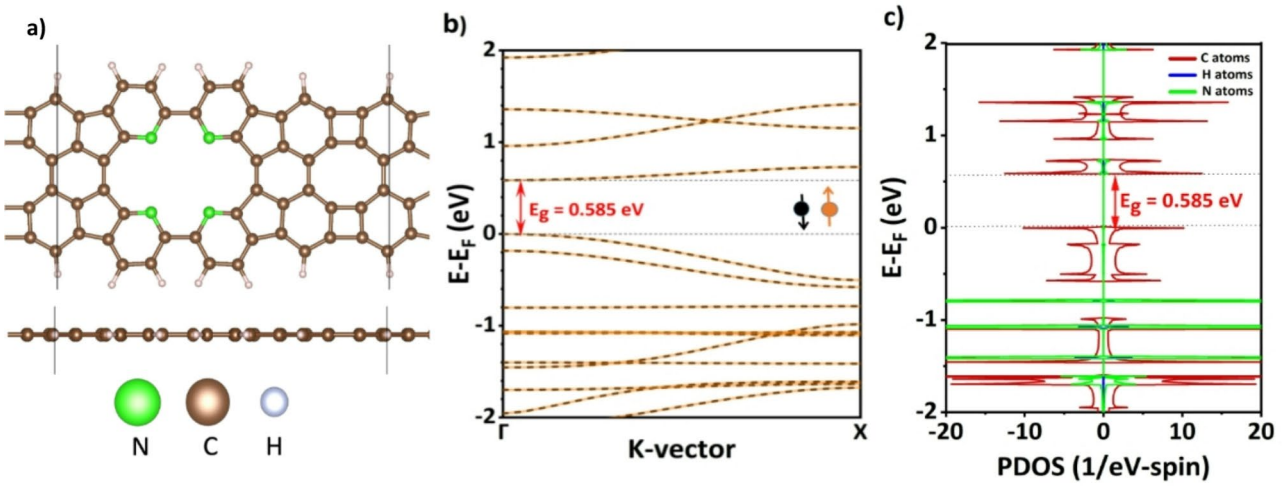

Fig. 1. Pristine carbon nanoribbon $C_{48}N_4$: (**a**) Optimized atomic structure in primitive cell (top and side views). (**b**) Band structure. (**c**) Spin-polarized partial density of states (PDOS). The Fermi level is taken as a reference ($E_F = 0$).

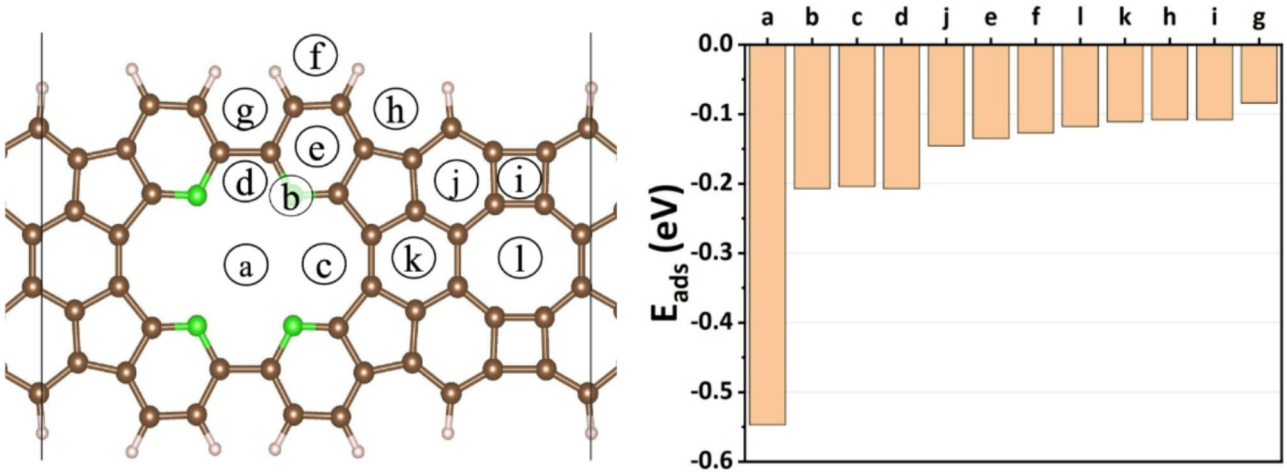

Fig. 2. Tested sites for active adsorption of N_2 gas molecule on carbon nanoribbon $C_{48}N_4$ and their corresponding adsorption energies (E_{ads}).

displayed in Fig. 4. The E_{ads} values are on the weaker side, especially in comparison to the interfering air molecules, thus not suitable for practical sensing applications.

It is worth stating that appropriate adsorption of the incident species is critical for the enhanced sensitivity of any sensor. Thus, VOCs must adsorb on N-CNRs with E_{ads} values capable of altering the electronic and magnetic properties of the latter. At the same time, E_{ads} should not be so strong that the desorption of the VOCs is impossible and the nanosensor becomes irreversible. Ideally, the E_{ads} VOCs should be between strong physisorption and weak chemisorption. Considering this, selected TMs (Co, Fe, Mn, Ni) have been incorporated into N-CNRs for the adsorption of VOCs on TMs-N-CNRs.

Adsorption of VOCs on TM-doped N-CNRs

To obtain TM-doped N-CNRs, selected TMs (Co, Fe, Mn, Ni) are adsorbed on N-CNRs at different binding sites and the corresponding binding energies (E_{bind}) are calculated. We observe that regardless of any initial configuration, all the TMs stabilize in the big pore of N-CNRs with significantly strong E_{bind} values of -6.00, -5.217, -5.594, and – 5.916 eV for Co, Fe, Mn, and Ni, respectively (Fig. S2). Strong E_{bind} values confirm isolated dispersion of incident TMs over N-CNRs without clustering. Furthermore, the thermal stability of TMs-N-CNRs is confirmed through ab initio molecular dynamics (AIMD) simulations at 1000 K and the systems remained stable for 9 picoseconds. The relaxed structures of TMs-N-CNRs are shown in Fig. S3 (supplementary information). It is worth noting that the TMs doping induced magnetism and more importantly changed the

VOCs	Pristine $C_{48}N_4$ NR ($M_o = 0.0\ \mu_B$)			Mn-doped ($M_o = 4.98\ \mu_B$)			Fe-doped ($M_o = 3.97\ \mu_B$)			Co-doped ($M_o = 2.96\ \mu_B$)			Ni-doped ($M_o = 2.00\ \mu_B$)		
	E_{ads} (eV)	M (μ_B)	$\lvert\Delta M\rvert$ (μ_B)	E_{ads} (eV)	M (μ_B)	$\lvert\Delta M\rvert$ (μ_B)	E_{ads} (eV)	M (μ_B)	$\lvert\Delta M\rvert$ (μ_B)	E_{ads} (eV)	M (μ_B)	$\lvert\Delta M\rvert$ (μ_B)	E_{ads} (eV)	M (μ_B)	$\lvert\Delta M\rvert$ (μ_B)
2-pentanone ($C_5H_{10}O$)	-0.50	0	0	-0.42	4.94	0.04	-0.80	4.03	0.06	-0.53	2.83	0.13	-0.39	1.94	0.06
Isoprene (C_5H_8)	-0.41	1.02	1.02	-0.79	5.00	0.02	-0.90	4.06	0.09	-0.73	3.14	-0.18	-0.18	1.89	0.11
Butanone (C_4H_8O)	-0.20	0	0	-0.73	4.92	0.06	-1.57	3.86	0.11	-0.98	2.93	0.03	-0.42	1.59	0.41
Methylglyoxal ($C_3H_4O_2$)	-0.06	2.12	2.12	-0.56	4.46	0.52	-1.26	3.80	0.17	-0.60	2.69	0.27	-0.01	1.56	0.44
N-decanal ($C_{10}H_{20}O$)	-0.74	0	0	-0.85	4.95	0.03	-1.48	4.00	0.03	-0.77	2.90	0.06	-0.79	1.98	0.02
N-pentanal ($C_5H_{10}O$)	-0.45	0	0	-0.36	4.93	0.05	-1.06	4.01	0.04	-0.54	2.85	0.11	-0.39	1.86	0.14
Pyridine (C_5H_5N)	-0.15	0	0	-0.60	5.00	0.02	-0.67	3.95	0.02	-0.10	2.83	0.13	-0.15	1.72	0.28

Table 1. Adsorption energy (E_{ads}), Magnetization (M) and the absolute value of change of magnetization ($|\Delta M|$) for the seven VOCs, related to GC biomarkers, on pristine and TM-doped N-CNRs.

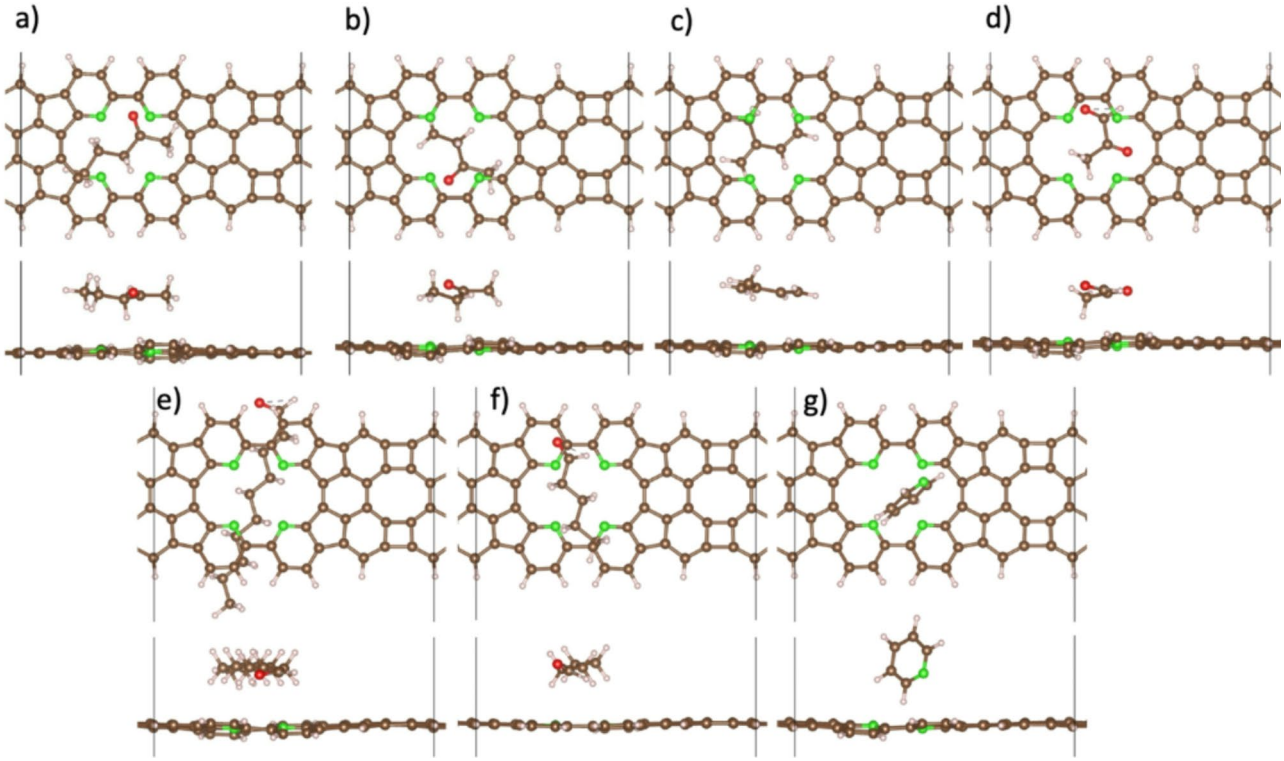

Fig. 3. Atomically relaxed structures of the seven VOCs, related to GC, on nitrogen functionalized CNRs: (**a**) 2-pentanone "$C_5H_{10}O$", (**b**) Butanone "C_4H_8O", (**c**) Isoprene "C_5H_8", (**d**) Methylglyoxal "$C_3H_4O_2$", (**e**) N-decanal "$C_{10}H_{20}O$", (**f**) N-pentanal "$C_5H_{10}O$", (**g**) Pyridine "C_5H_5N". Color code: C (brown), H (pink), O (red), N (green).

character of TMs-N-CNRs from paramagnetic semiconductor to ferromagnetic metal, as displayed by the spin-polarized band structures and PDOS in Fig. S4 (supplementary information).

After obtaining the relaxed geometries, we introduce each of the VOCs on TM-doped N-CNRs and the systems are completely optimized until the global minimum energy is achieved. Figure 5; Table 1 show the calculated E_{ads} values for the seven VOCs on TM-doped N-CNRs. It clearly shows that TMs-N-CNRs enhanced E_{ads} to the limit to achieve selective adsorption of VOCs as compared to the interfering air molecules. Particularly, Fe-doped N-CNR (N-CNR: Fe) results in the strongest E_{ads} values of -0.802, -0.899, -1.566, -1.260, -1.482, -1.057, and − 0.674 eV for 2-pentanone, butanone, isoprene, methylglyoxal, N-decanal, N-pentanal, and pyridine, respectively.

The Selectivity of the TM-doped N-CNRs based nano-sensor is studied by comparing the E_{ads} values of VOCs with those of interfering air molecules. For example, we find that the common molecules, H_2O and N_2 result in E_{ads} values of -0.613, and − 0.547 eV, respectively. Whereas all the VOCs yield stronger E_{ads} values on TM-doped N-CNRs. Particularly, isoprene, methylglyoxal, N-decanal, and N-pentanal yield much stronger adsorption character, which indicates their selective detection in the presence of interfering air molecules. These E_{ads} are promising and cause measurable changes in the electronic and magnetic properties of N-CNR: Fe, which is a prerequisite for an efficient sensing mechanism.

Band structures and density of states (DOS)

Based on the adsorption mechanism, four VOCs, namely, isoprene, methylglyoxal, N-decanal, and N-pentanal possess E_{ads} > 1.00 eV on N-CNR: Fe, as shown in Table 1. Therefore, we considered only these VOCs for further analysis. Nevertheless, the electronic structures, spin-polarized bands, partial density of states (PDOS), and relaxed configurations of all the seven VOCs on N-CNR: Fe are presented in Fig. 6. In the band structures, the bands of spin-down states are in solid orange lines while those of spin-up states are in dotted black curves.

Before the adsorption of the VOCs, the spin-polarized band structure and PDOS of N-CNR: Fe, presented in Fig. 6, clearly shows a half-metallicity, where spin-down states are semiconducting ($E_g^{\downarrow}$ = 0.227 eV) and spin-up states are metallic (see Table 2). The near Fermi states look hybrid due to covalent character mixing between C(p) and Fe(d) states. After the VOCs adsorption the band structures of N-CNR: Fe exhibit some changes especially near the Fermi level. The common trends caused by VOCs adsorptions can be summarized as follows: (i) Half metallicity is maintained with spin-up states being semiconducting while spin-down being metallic (see Table 2), but the characters of contributing states have changed. (ii) Mainly the valence-band maximum (VBM) and the conduction-band minimum (CBM) states in the spin-up semiconducting states are attributed to carbon C(p) orbitals, while the metallic spin-down states are attributed to Fe(d) orbitals more than C(p) orbitals. Such

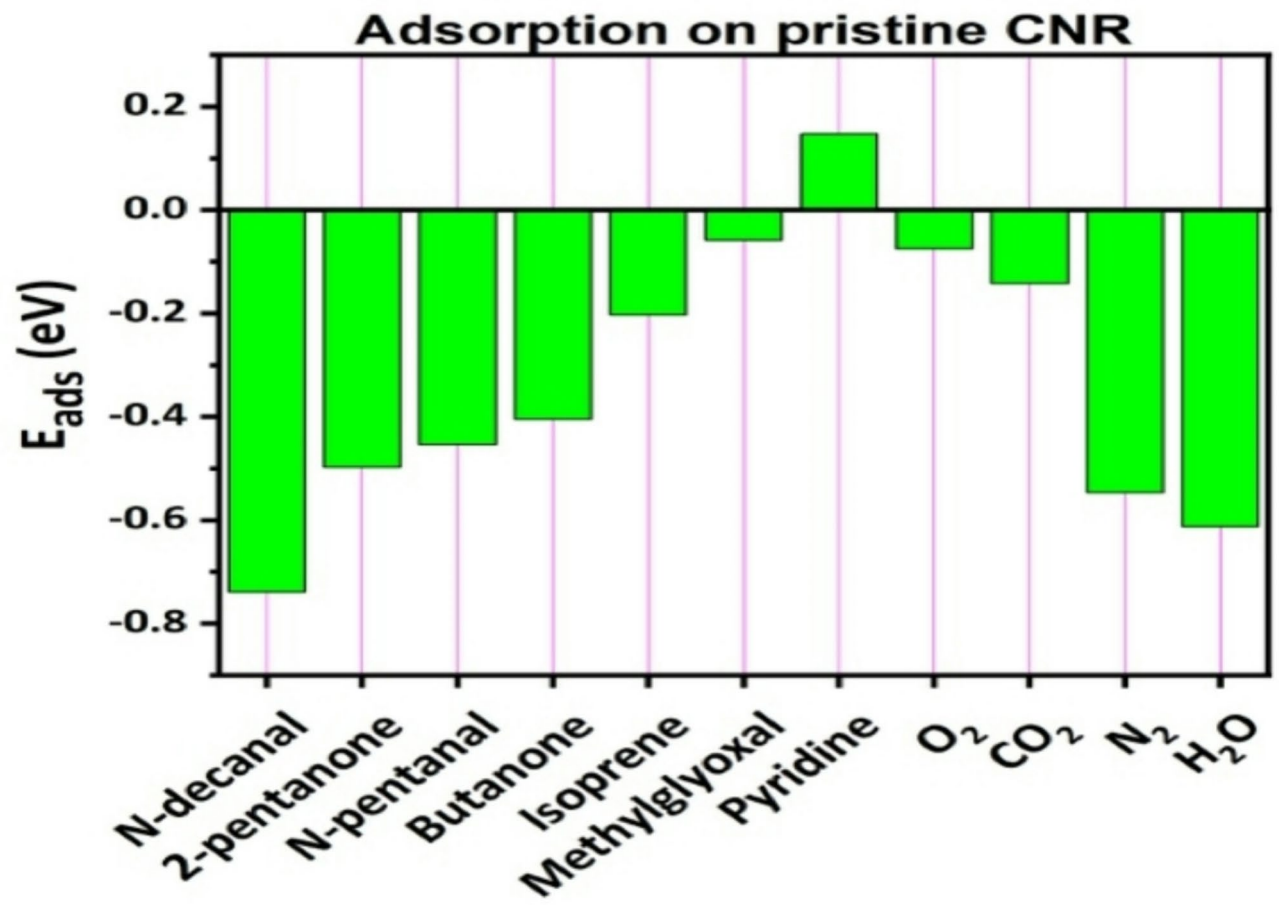

Fig. 4. Adsorption energies of seven VOCs, related to GC biomarkers, on nitrogen functionalized CNRs (N-CNRs).

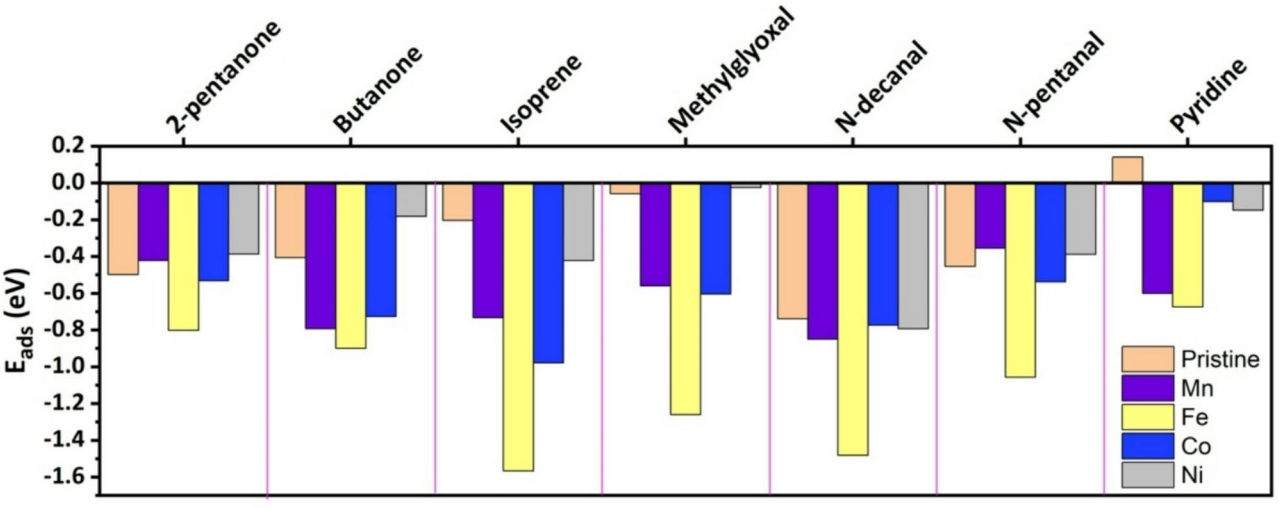

Fig. 5. Adsorption energies of seven VOCs, related to GC, on pristine and TM-doped M@CNRs (with TM = Mn, Fe, Co, and Ni).

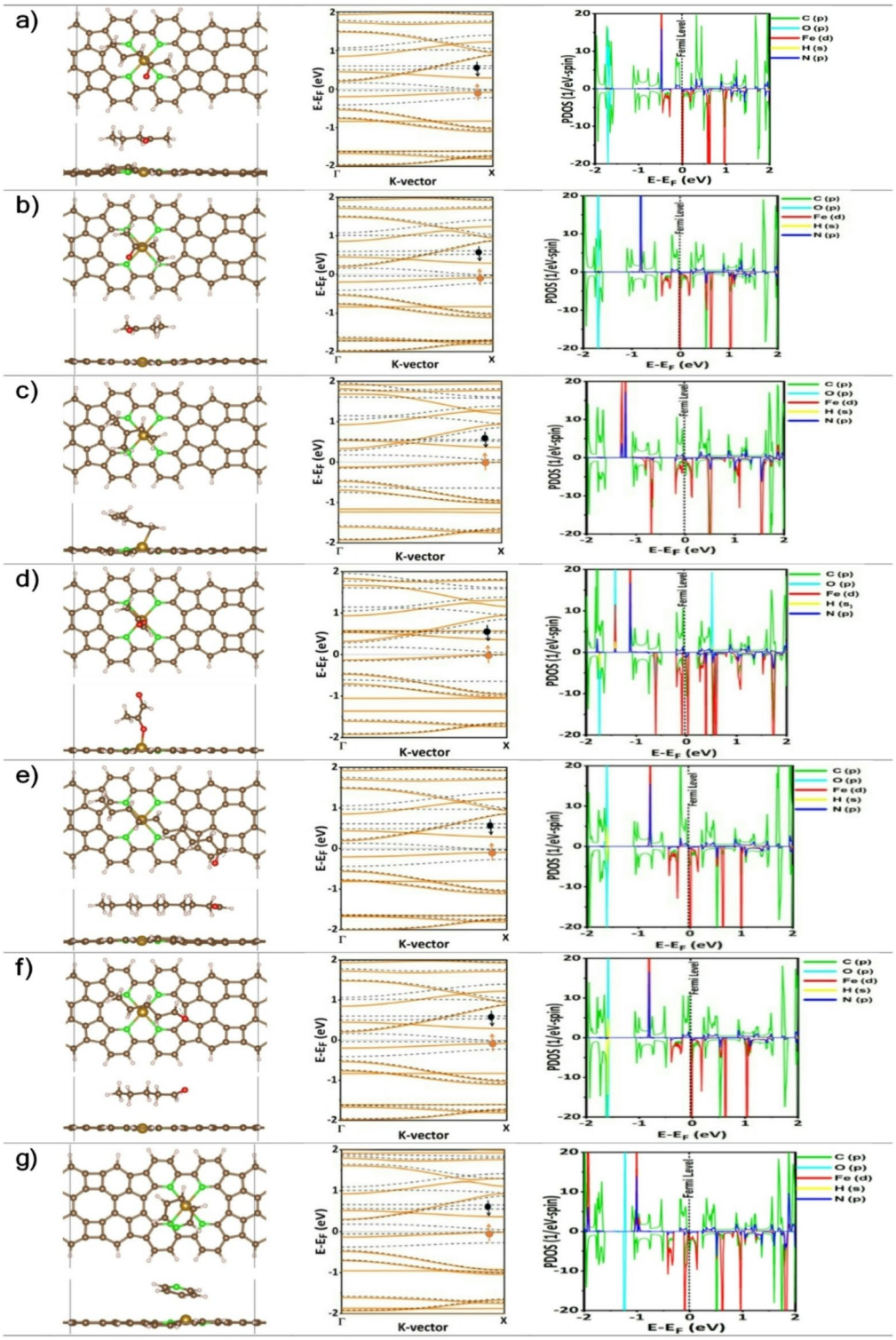

Fig. 6. Atomically relaxed structures of seven VOCs, related to GC biomarkers, on N-CNR: Fe (Top and side views) and partial density of states (PDOS): (**a**) 2-pentanone "$C_5H_{10}O$", (**b**) Butanone "C_4H_8O", (**c**) Isoprene "C_5H_8", (**d**) Methylglyoxal "$C_3H_4O_2$", (**e**) N-decanal "$C_{10}H_{20}O$", (**f**) N-pentanal "$C_5H_{10}O$", (**g**) Pyridine "C_5H_5N". In band structures spin-up and spin-down states are shown in solid-orange and small-dashed black lines, respectively. In both bands and PDOS, the Fermi level is taken as an energy reference ($E_F = 0$). Color code for atoms: C (brown), O (red), N (green), and H (pink).

VOCs	E_{ads}(eV)	d (Å)	$E_g^{\uparrow}$ (eV)	$E_g^{\downarrow}$(eV)	Property	Δq (e)	τ (sec)
Pristine CNR	N/A	N/A	0.0	0.227	H/M	N/A	N/A
2-pentanone	-0.802	2.44	0.278	0.0	H/M	-0.098	8.554
Butanone	-0.899	2.48	0.281	0.0	H/M	-0.073	414.218
Isoprene	-1.566	1.85	0.331	0.0	H/M	-0.207	1.60×10^{14}
Methylglyoxal	-1.260	1.89	0.318	0.0	H/M	-0.447	7.73×10^{8}
N-decanal	-1.482	2.56	0.288	0.0	H/M	-0.251	5.56×10^{12}
N-pentanal	-1.057	2.39	0.298	0.0	H/M	-0.115	2.30×10^{8}
Pyridine	-0.674	2.19	0.320	0.0	H/M	-0.088	0.051
H_2O	-0.760	2.34	0.279	0.0	H/M	-0.012	1.590
O_2	-0.566	3.00	0.085	0.0	H/M	-0.160	6.79×10^{-4}
CO_2	-0.518	2.28	0.303	0.0	H/M	-0.367	9.96×10^{-5}
N_2	-0.768	3.30	0.272	0.0	H/M	-0.009	2.195

Table 2. Adsorption energy (E_{ads}), adsorption distance (d), Bandgap energies of spin-up and spin-down states ($E_g^{spin-up}$ and $E_g^{spin-down}$), charge transfer (Δq), and recovery time (τ) of the seven VOCs, related to GC, and interfering air molecules on Fe-doped carbon nanoribbon (N-CNRs:Fe).

characteristics should be attributed to the strong charge exchange between VOCs and N-CNR: Fe, where the former is playing the role of oxidizing molecules. Table 2 shows the charge exchange calculated by Bader charge analysis to be about Δq = -0.207 e, -0.447 e, -0.251 e and − 0.115 e for isoprene, methylglyoxal, N-decanal, and N-pentanol, respectively. (iii) The atomic structures shown in Fig. 6b, c, d, e display two chemisorption and two physisorption processes, respectively.

It is important to explain the existence of half-metallicity in the N-CNR: Fe, which has a length of a = 16.190 Å and under a periodic boundary that is within the critical length for ferromagnetic interactions with the mirror images of the Fe dopants. Such ferromagnetic coupling (FMC) should be the reason for the half-metallicity. In our recent work on TMs embedded C_2N, we estimated the critical length for the existence of FMC interactions to be about $L_c \approx$ 21–29 Å[45]. The half metallicity in the case of Fe embedment in C_2N big pore was observed in double atom catalyst (DAC) and was attributed to both FMC interactions with images of DAC through PBCs and the synergetic effects[45]. Another study[46] reported half-metallicity in TM-doped transition metal dichalcogenides (TMDs) (MoX_2, X = S, Se) monolayers. Specifically, half-metallicity existed in small-sized samples of (Mn, Fe, and Ni)-doped MoS_2 and (V, Mn, Fe, and Co)-doped $MoSe_2$ when the supercells were smaller than 6 × 6 primitive cells. Thus, the present findings of half-metallicity are in excellent agreement with literature[45,46]. It is worth mentioning that half-metallicity exists in N-CNR: Fe even after the adsorption of VOCs, therefore it should not be considered as a parameter of selectivity.

Charge density difference (CDD) and work function

Figure 7 illustrates the charge-density difference (CDD) before and after the adsorption of VOCs in N-CNR: Fe. The gain (deficit) in charge is indicated by yellow (cyan) color. The charge transfer is calculated using the Bader analysis and results are shown in Table 2. The atomic relaxations are associated with charge transfers from the N-CNR: Fe to VOCs. As Fe in N-CNR: Fe is contributing with major states at Fermi level, all the VOCs and interfering air molecules seem to act as oxidizing entities. Moreover, stronger adsorption is associated with the greater charge transfer from N-CNR: Fe to the VOCs. Amongst the four VOCs predicted to have the highest selectivity, methylglyoxal is distinguished having a chemisorption, forming a chemical bond with N-CNR: Fe (d = 1.89 Å) and resulting in the highest charge transfer (Δq = -0.447 e). Figure 8 displays the results of absolute values of E_{ads} and charge transfer of the studied VOCs and interfering air molecules on N-CNR: Fe.

Among all, isoprene, methylglyoxal, N-decanal, and N-pentanal show enhanced selectivity. Figure 9 displays the work functions (ϕ) of N-CNR: Fe before and after the adsorption of VOCs. With a clear distinction, the methylglyoxal results into the largest ϕ. This is consistent with the large charge transfer accumulated by methylglyoxal from N-CNR: Fe. It seems that the electrons build up a strong bond between methylglyoxal and the N-CNR: Fe and the effects on Fermi states should be the largest. Hence, such strong interaction would have the largest effect on transport properties and consequently the sensor response.

Half-metallicity, recovery time, and selectivity

The embedment of TMs on N-CNRs has induced several changes in the electronic and magnetic properties. After the doping, N-CNR: Fe transforms not only into ferromagnetic metallic but also with half-metallic characters. As elaborated above, the origins of the half-metallicity characters are attributed to the existence of FMC between the TMs and their mirror images[45,46]. Half-metallicity is a fundamental property required in spintronic device applications and it takes place when one spin state is metallic while the other is semiconducting (i.e., the electric current becomes spin-polarized). Table 2 shows E_g of spin-up and spin-down states before and after the adsorption of the VOCs and interfering air molecules on N-CNR: Fe. It seems that half metallicity is rebooted as being mainly controlled by FMC interactions. Before the adsorption of the VOCs, spin-up states in N-CNR: Fe are conductive while the spin-down states are semiconducting with an indirect $E_g^{\downarrow}$ of 0.227 eV. After the adsorptions of VOCs and air molecules, N-CNR: Fe remains half-metallic and persists to maintain

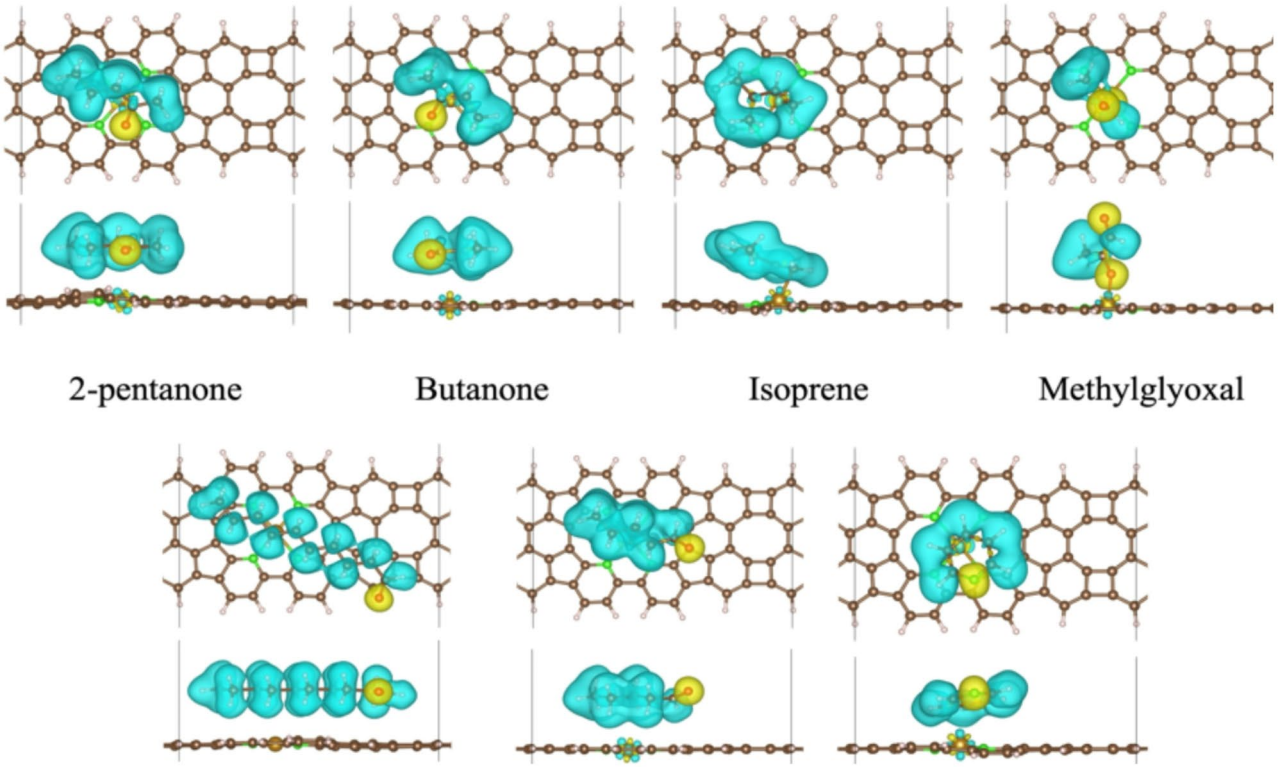

Fig. 7. Charge density difference (CDD) showing the bond characteristics of maximally localized Wannier functions (MLWFs) of the seven VOCs, related to GC biomarkers, on N-CNRs: Fe. Yellow and Cyan iso-surfaces indicate charge aggregation and depletion, respectively. The iso-surfaces level is 0.03 e/Bohr^3.

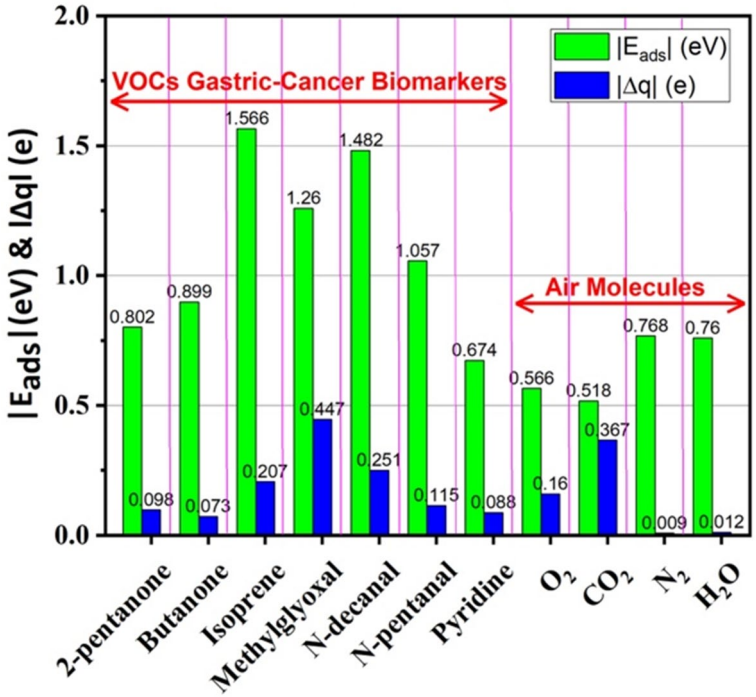

Fig. 8. Summary of absolute values of adsorption energies and charge transfers of seven VOCs, related to GC biomarkers, and interfering air molecules on N-CNR:Fe.

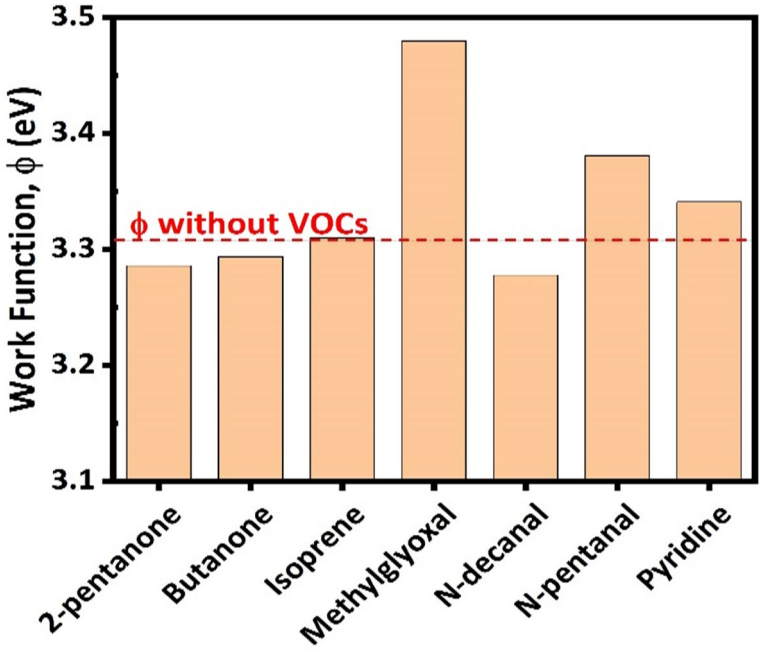

Fig. 9. Work function (in eV units) before (horizontal dashed line) and after (histograms) the adsorption of seven VOCs, related to GC biomarkers, on N-CNR: Fe.

the spin-down metallic and spin-up is semiconducting with also an indirect $E_g^{\uparrow}$ of 0.281–0.331 eV, as shown in Table 2. It appears that TM-doped N-CNRs induced magnetism (magnetization values are given in Table 1) rather than half-metallicity, however, both properties remain rebooted and do not get perturbed by the VOCs adsorption, especially in the TM-doped samples, which are used as adsorbent substrates. Notably, there are two VOCs (butanone and methylglyoxal) that can induce magnetizations of 1.02 μ_B and 2.12 μ_B into the pristine samples. Otherwise, all VOCs would not change the magnetic states of the doped sample and the half-metallicity characters are rebooted.

An important parameter for reversible sensing is the recovery time (τ). Table 2 shows the recovery times for all the seven VOCs and four interfering molecules. It is evident from Eq. (5) that τ mainly depends on E_{ads} values. Among the studied VOCs, isoprene, and methylglyoxal result in comparatively strong E_{ads} values of -1.566 and − 1.260 eV, respectively and the corresponding τ values are significantly high. However, it is worth mentioning that τ values are calculated under visible-light exposure and at room temperature (300 K). At elevated temperatures, τ values could be significantly reduced to a reasonable range.

Conclusions

Spin-polarized DFT calculations were employed to study the adsorption properties of the seven VOCs related to GC versus four interfering air molecules (N_2, O_2, H_2O, CO_2) on a recently synthesized CNRs composed of 4-5-6-8-membered rings. The adsorptions of the VOCs on nitrogen functionalized CNRs, (N-CNRs) yielded weak E_{ads} values. To enhance the adsorption mechanism and selectivity, selected TMs (Co, Fe, Mn, Ni) were embedded in the central pore of N-CNRs to form N-CNRs: TM. It was observed that incorporations of all the TMs improved the adsorption mechanism, however N-CNR: Fe enhanced the E_{ads} values to -0.802, -0.899, -1.566, -1.260, -1.482, -1.057, and − 0.674 eV for 2-pentanone, butanone, isoprene, methylglyoxal, N-decanal, N-pentanal, and pyridine, respectively. Although N-CNR: Fe absorbed all the VOCs appropriately, enhanced selectivity was observed for isoprene, methylglyoxal, N-decanal, and N-pentanal. Suitable E_{ads} values coupled with measurable changes in the electronic and magnetic properties, which were calculated through band structures, the density of states, work function and charge transfer analysis, authenticated the potential of N-CNR: Fe as an efficient biosensor towards GC-related VOCs.

Computational method

We employed DFT as incorporated in the Vienna Ab-initio Simulation Package (VASP)[47] to study the adsorption of seven VOCs related to GC, versus interfering air molecules (N_2, O_2, H_2O, CO_2) on CNRs, and TM-doped N-CNRs. It can be seen in Fig. 1a that N-CNR has a rectangular-lattice primitive cell. Vacuum spaces of 10 Å and 15 Å were inserted along y and z directions, respectively, to ensure the isolation from the mirror images produced by periodic boundary conditions. Linearized augmented plane wave (LAPW) was used as a basis set with an energy cut off 500 eV, while Perdew-Burke-Ernzerhof (PBE)[48] was used to describe the exchange-correlation functional within the generalized gradient approximation (GGA). To describe the van der Waals interactions, we used Grimme's DFT-D3 scheme[49]. In the Brillouin zone integration, we used the special-point technique of Monkhorst-Pack[50], with k-point grids of 3 × 1 × 1 and 5 × 1 × 1 for atomic relaxation and density of

states calculations, respectively. As convergence criteria, we used tolerances of 10^{-6} eV and 10 meV/Å for energy and forces, respectively. For charge transfer, Bader charge analysis used[51] and charge-density difference (CDD) incorporated in VASP.

Based on total energy calculations, binding energy (E_{bind}) of embedment of TMs (Co, Fe, Mn, Ni) in N-CNRs was calculated by the following,

$$E_{bind} = E_{TMs-N@CNRs} - E_{N@CNRs} - E_{TMs} \tag{1}$$

where the first, second, and third terms represent the total energies of N-CNRs loaded with TMs, bare N-CNRs, and TMs, respectively.

The adsorption energy (E_{ads}) of the VOCs and interfering air molecules on TM-doped N-CNRs were calculated using the following formula:

$$E_{ads} = E_{TMs-N@CNRs-gas} - E_{TMs-N@CNRs} - E_{gas} \tag{2}$$

where first, second, and third terms represent total energies of TM-doped N-CNRs loaded with VOCs/air molecules, bare TM-doped N-CNRs and those of VOCs/air molecules, respectively.

The magnetization can be calculated using the results of spin-polarized TDOS as follows[52].

$$M = \mu_B \int_{-\infty}^{E_F} \left[G_{tot}^{\uparrow}(E) + G_{tot}^{\downarrow}(E) \right] dE \tag{3}$$

where E_F is Fermi energy, $G_{tot}^{\uparrow}(E)$ and $G_{tot}^{\downarrow}(E)$ are spin-polarized TDOS of spin-up and spin-down states, respectively, while μ_B stands for Bohr's magneton. It should be emphasized that it is customary to present $G_{tot}^{\downarrow}(E)$ negative and the total density of states $G_{tot}(E) = G_{tot}^{\uparrow}(E) - G_{tot}^{\downarrow}(E)$ to be normalized to yield the total number of valence electrons in the system (N):

$$N = \int_{-\infty}^{E_F} \left[G_{tot}^{\uparrow}(E) - G_{tot}^{\downarrow}(E) \right] dE \tag{4}$$

For example, before the incorporation of the TM catalyst the $C_{48}N_4H_{12}$ nanoribbon, comprised of 64 atoms, should contain a total of 224 electrons (48 C + 4 *N* + 12 H = 48 × 4 + 4 × 5 + 12 × 1 = 224 electrons). Within VASP, the pseudopotentials of the TM-SAC atoms describe the outer shells of electrons (e.g., Mn, Fe, Co, and Ni contain $3s$[53], $3d^X$, with X = 5, 6, 7, 8, respectively). So, the valence electrons of these respective TM-SAC atoms should be 7, 8, 9, and 10, respectively. Consequently, the total number of electrons in the system should be 231–234 electrons, respectively.

To assess whether the gas sensor should be reusable or disposable, it is important to calculate the recovery time. Within the framework of the conventional transition-state theory, recovery time can be expressed as follows[54]:

$$\tau = \upsilon_o^{-1} \exp\left[-\frac{E_{ads}}{k_B T} \right] \tag{5}$$

where E_{ads}, k_B and T are the adsorption energy, Boltzmann constant (8.62×10^{-5} eV/K) and the absolute temperature, respectively. υ_0 is the attempt frequency having values 10^{12} and 10^{16} Hz under visible and UV light situations, respectively[55,56]. In this investigation, we used the value $\upsilon_0 = 10^{12}$ Hz to estimate the recovery time under exposure to visible light and in ambient conditions.

Data availability

The datasets used and/or analyzed during the current study are available from the corresponding author on reasonable request.

Received: 12 September 2024; Accepted: 4 April 2025
Published online: 16 April 2025

References

1. Conti, C. B. et al. Early gastric cancer: update on prevention, diagnosis and treatment. *Int. J. Environ. Res. Public. Health*. **20**, 2149 (2023).
2. Zhang, J. et al. Breath volatile organic compound analysis: An emerging method for gastric cancer detection. *J. Breath. Res.* **15**, 044002 (2021).
3. Jung, Y. J. et al. Advanced diagnostic technology of volatile organic compounds real-time analysis from exhaled breath of gastric cancer patients using proton-transfer-reaction time-of-flight mass spectrometry. *Front. Oncol.* **11**, 560591 (2021).
4. Chung, J. et al. Diagnosis by volatile organic compounds in exhaled breath from patients with gastric and colorectal cancers. *Int. J. Mol. Sci.* **24**, 129 (2022).
5. Wang, L. et al. Volatile organic compounds as a potential screening tool for neoplasm of the digestive system: A meta-analysis. *Sci. Rep.* **11**, 23716 (2021).

6. Cai, Y. et al. Noninvasive analysis of exhaled breath for gastric cancer diagnosis using paper-based smartphone nano-optoelectronic noses. *Sens. Actuat. B Chem.* **381**, 133411 (2023).
7. Mochalski, P. et al. Ex vivo emission of volatile organic compounds from gastric cancer and non-cancerous tissue. *J. Breath. Res.* **12**, 046005 (2018).
8. Huang, L. et al. Noninvasive diagnosis of gastric cancer based on breath analysis with a tubular surface-enhanced Raman scattering sensor. *ACS Sens.* **7**, 1439–1450 (2022).
9. Perfecto, T. M., Zito, C. A. & Volanti, D. P. Effect of NiS nanosheets on the Butanone sensing performance of ZnO Hollow spheres under humidity conditions. *Sens. Actuat. B Chem.* **334**, 129684 (2021).
10. Hong, Y. et al. Exhaled breath analysis using online preconcentration mass spectrometry for gastric cancer diagnosis. *J. Mass. Spect.* **56**, e4588 (2021).
11. Mochalski, P. et al. Identification of key volatile organic compounds released by gastric tissues as potential non-invasive biomarkers for gastric cancer. *Diagnostics* **13**, 335 (2023).
12. Bac, P. T. V., Lam, P. T. & An, D. V. *VNU J. Sci. Math. Phys.* **36**, 71–79 (2020).
13. Bhuvaneswari, R., Nagarajan, V. & Chandiramouli, R. Chemiresistive β-Tellurene nanosheets for detecting 2-Butanone and 2-Pentanone-a first-principles study. *Mater. Today Commun.* **26**, 101758 (2021).
14. Novoselov, K. S. et al. Electric field effect in atomically thin carbon films. *Science* **306**, 666–669 (2004).
15. Geim, A. K. & Novoselov, K. S. The rise of graphene. *Nat. Mater.* **6**, 183–191 (2007).
16. Kong, D. et al. Synthesis of MoS_2 and $MoSe_2$ films with vertically aligned layers. *Nano Lett.* **13**, 1341–1347 (2013).
17. You, J., Hossain, M. D. & Luo, Z. Synthesis of 2D transition metal dichalcogenides by chemical vapor deposition with controlled layer number and morphology. *Nano Conv.* **5**, 26 (2018).
18. Naguib, M. et al. Two-dimensional nanocrystals produced by exfoliation of Ti_3AlC_2. *Adv. Mater.* **23**, 4248–4253 (2011).
19. Gogotsi, Y. & Anasori, B. The rise of MXenes. *ACS Nano* **13**, 8491–8494 (2019).
20. Mahmood, J. et al. Nitrogenated Holey two-dimensional structures. *Nat. Commun.* **6**, 6486 (2015).
21. Xu, J. et al. 2D frameworks of C_2N and C_3N as new anode materials for lithium-ion batteries. *Adv. Mater.* **29**, 1702007 (2017).
22. Cai, X. et al. Novel 2D porous C_3N_2 framework as a promising anode material with ultra-high specific capacity for lithium-ion batteries. *J. Mater. Chem. A* **10**, 6551–6559 (2022).
23. Humayun, M., Israr, M., Khan, A. & Bououdina, M. State-of-the-art single-atom catalysts in electrocatalysis: From fundamentals to applications. *Nano Energy* **113**, 108570 (2023).
24. Cheng, N., Zhang, L., Doyle-Davis, K. & Sun, X. Single-atom catalysts: From design to application. *Electrochem. Energy Rev.* **2**, 539–573 (2019).
25. Hu, H. et al. Stability of single-atom catalysts for electrocatalysis. *J. Mater. Chem. A* **10**, 5835–5849 (2022).
26. Gloag, L., Somerville, S. V., Gooding, J. J. & Tilley, R. D. Co-catalytic metal–support interactions in single-atom electrocatalysts. *Nature Rev. Mater.* **9**, 173–189 (2024).
27. Li, J. et al. Challenges and perspectives of single-atom-based catalysts for electrochemical reactions. *JACS Au* **3**, 736–755 (2023).
28. Hussain, M. I. et al. Single-atom catalysts for electrocatalytic applications: Synthetic strategies, in-situ characterization, and future challenges. *Appl. Mater. Today* **36**, 102037 (2024).
29. Gong, X. et al. Heterogeneous single-atom catalysts for energy process: recent progress, applications and challenges. *Energy Mater.* **3**, 200016 (2023).
30. Chu, T. et al. Progress and perspectives of single-atom catalysts for gas sensing. *Adv. Mater.* **35**, 2206783 (2023).
31. Lei, G. et al. Emerging single-atom catalysts in gas sensors. *Chem. Soc. Rev.* **51**, 7260–7280 (2022).
32. Zhou, L., Tian, P., Zhang, B. & Xuan, F. Z. Data-driven rational design of single-atom materials for hydrogen evolution and sensing. *Nano Res.* **17**, 3352–3358 (2024).
33. Ma, W., Wan, H., Zhang, L., Zheng, J. Y. & Zhou, Z. Single-atom catalysts for electrochemical energy storage and conversion. *J. Energy Chem.* **63**, 170–194 (2021).
34. Shah, S. S. A. et al. Single-atom catalysts for next-generation rechargeable batteries and fuel cell. *Energy Storage Mater.* **45**, 301–322 (2022).
35. Li, X. et al. Single-atom catalyst application in distributed renewable energy conversion and storage. *SusMat* **3**, 160–179 (2023).
36. Tian, H. et al. Single-atom catalysts for high-energy rechargeable batteries. *Chem. Sci.* **12**, 7656–7676 (2021).
37. Hong, Q. et al. Adaptable graphitic C_6N_6-based copper single-atom catalyst for intelligent biosensing. *Nat. Commun.* **14**, 2780 (2023).
38. Chellasamy, G. et al. Single-atom catalysts for biosensing: progress in theoretical and mechanistic Understanding. *Coord. Chem. Rev.* **502**, 215606 (2024).
39. Xiang, H., Feng, W. & Chen, Y. Single-atom catalysts in catalytic biomedicine. *Adv. Mater.* **32**, 1905994 (2020).
40. Fan, Y., Liu, S., Yi, Y., Rong, H. & Zhang, J. Catalytic nanomaterials toward atomic levels for biomedical applications: from metal clusters to single-atom catalysts. *ACS Nano* **15**, 2005–2037 (2021).
41. Alfalasi, W., Hussain, T. & Tit, N. Ab-initio investigation of titanium carbide MXenes to tune the detection of lung cancer biomarkers. *Sci. Rep.* **14**, 1403 (2024).
42. Alfalasi, W. & Tit, N. Efficient detection of lung cancer biomarkers using functionalized transition metal dichalcogenides (MoS_2) monolayers: DFT study. *FlatChem* **45**, 100651 (2024).
43. Kang, F., Sun, L., Gao, W., Sun, Q. & Xu, W. On-surface synthesis of a carbon nanoribbon composed of 4-5-6-8-membered rings. *ACS Nano* **17**, 8717–8722 (2023).
44. Mortazavi, B. A theoretical investigation of the structural, electronic and mechanical properties of pristine and nitrogen-terminated carbon nanoribbons composed of 4-5-6-8-membered rings. *J. Comp. Sci.* **7**, 269 (2023).
45. Khan, S., Feng, Y. P. & Tit, N. Synergetic effects of combining TM single-and double-atom catalysts embedded in C_2N on inducing half-metallicity: DFT study. *2D Mater.* **10**, 015016 (2022).
46. Alfalasi, W., Feng, Y. P. & Tit, N. Designing a functionalized 2D-TMD (MoX_2, X = S, Se) hosting half-metallicity for selective gas-sensing applications: Atomic-scale study. *Acta Mater.* **246**, 118655 (2023).
47. Kresse, G. & Furthmüller, J. Efficient iterative schemes for Ab initio total-energy calculations using a plane-wave basis set. *Phys. Rev. B* **54**, 11169–11186 (1996). https://www.vasp.at
48. Perdew, J. P., Burke, K. & Ernzerhof, M. Generalized gradient approximation made simple. *Phys. Rev. Lett.* **77**, 3865 (1996).
49. Grimme, S., Antony, J., Ehrlich, S. & Krieg, H. A consistent and accurate Ab initio parametrization of density functional dispersion correction (DFT-D) for the 94 elements H-Pu. *J. Chem. Phys.* **132**, 154104 (2010).
50. Monkhorst, H. J. & Pack, J. D. Special points for Brillouin-zone integrations. *Phys. Rev. B* **13**, 5188–5192 (1976).
51. Henkelman, G., Arnaldsson, A. & Jónsson, H. A fast and robust algorithm for bader decomposition of charge density. *Comput. Mater. Sci.* **36**, 354–360 (2006).
52. Khan, S., Wasfi, A., Mushtaq, M., Awwad, F. & Tit, N. Transition-metal single atom catalyst embedded in C_2N for toxic-gas reduction reaction and selective gas-sensing application: Atomic-scale study. *Appl. Surf. Sci.* **599**, 154037 (2022).
53. Morgan, E. et al. The current and future incidence and mortality of gastric cancer in 185 countries, 2020–40: A population-based modelling study. *eClinicalMedicine* **47**, 101404 (2022).
54. Zhang, Y. H. et al. Improving gas sensing properties of graphene by introducing dopants and defects: A first-principles study. *Nanotechnology* **20**, 185504 (2009).

55. Aasi, A., Bajgani, S. E. & Panchapakesan, B. A first-principles investigation on the adsorption of Octanal and Nonanal molecules with decorated monolayer WS_2 as promising gas sensing platform. *AIP Adv.* **13**, 025157 (2023).
56. Aasi, A., Aghaei, S. M. & Panchapakesan, B. Nobel metal (Pt or Pd)-decorated atomically thin MoS_2 as a promising material for sensing colorectal cancer biomarkers through exhaled breath. *Int. J. Comput. Mater. Sci. Eng.* **13**, 2350014 (2024).

Acknowledgements
The authors sincerely thank Dr. Thomas Fowler for his valuable critical review of the manuscript. Additionally, our thanks extend to the National Water and Energy Centre (NWEC) at the UAE University for their generous financial support from grant number 12R162.

Author contributions
I.A.: Data curation, Investigation, Methodology, Validation, Visualization, Writing – Reviewing and editing. T.H.: Conceptualization, Data curation, Formal analysis, Validation, Writing – Reviewing and editing. S.N.: Data curation, Investigation, Writing – Reviewing and editing. N.T.: Conceptualization, Formal analysis, Funding acquisition, Project administration, Resources, Writing – original draft, Writing: reviewing and editing, Supervision.

Declarations

Competing interests
The authors declare no competing interests.

Additional information
Supplementary Information The online version contains supplementary material available at https://doi.org/10.1038/s41598-025-97518-x.

Correspondence and requests for materials should be addressed to N.T.

Reprints and permissions information is available at www.nature.com/reprints.

Publisher's note Springer Nature remains neutral with regard to jurisdictional claims in published maps and institutional affiliations.